Timescale-normalized fMRI reveals disrupted dynamic signal-energy balance in schizophrenia

Sir-Lord Wiafe[1], Spencer Kinsey[1], Najme Soleimani[1], Raymond O. Nsafoa[2], Nigar Khasayeva[1], Amritha Harikumar[1], Robyn Miller[1*], Vince D. Calhoun[1]

[1]Tri-Institutional Center for Translational Research in Neuroimaging and Data Science (TReNDS), Georgia State University, Georgia Institute of Technology, and Emory University, Atlanta, GA 30303, USA. [2]Kwame Nkrumah University of Science and Technology (KNUST) Hospital, Kumasi, 00233, Ghana

Abstract

Neural systems operate across diverse and nested timescales: fast unimodal fluctuations are gradually integrated within higher-order transmodal networks, complicating direct comparison of regional activity. We propose a systems principle of timescale normalization for coordinated signal-energy balance, in which healthy brains reconcile variable internal clocks so that inter-regional activity remains energetically proportionate over time. To operationalize this principle, we time-align regional fMRI signals via a time-resolved dynamic time-warping method that removes temporal distortions and isolates moment-to-moment amplitude differences. The residual amplitudes define a dynamic signal-energy disparity metric, quantifying coordination across intrinsic networks. Validation in the Human Connectome Project cohort (n = 1,200) demonstrated robust adherence to this system principle. Applied to a multi-site schizophrenia cohort (controls=160, patients=151), the approach revealed more heterogeneous signal-energy disparities in patients, particularly during faster fluctuations. State-switching analyses further showed that patients occupied and re-entered less balanced configurations more frequently, characterized by reduced spectral gap and longer mixing time, indicating slower re-stabilization of balanced energy states, greater heterogeneity and sluggish re-stabilization were associated with higher symptom severity and poorer working memory and reasoning. In summary, schizophrenia reflects a breakdown of timescale normalization, producing heterogeneous disparities in signal energy and impaired recovery of balanced network states. These findings establish dynamic signal-energy balance as a core systems mechanism directly linked to symptoms, cognition, and potential intervention monitoring.

Keywords: Time normalization, dynamic time warping, schizophrenia, high-frequency BOLD.

1. INTRODUCTION.

The human brain, despite constituting about 2% of the body's mass, consumes roughly 20% of its total energy[1], a cost driven by intensive neuronal processing and synaptic activity essential for complex cognitive functions[2]. Functional magnetic resonance imaging (fMRI) indexes this demand indirectly via the blood-oxygenation-level-dependent (BOLD) signal, reflecting neurovascular responses that accompany neural activation[2,3]. Although BOLD is not a direct measure of brain activity, converging work shows that larger BOLD amplitudes typically track increases in underlying energetic requirements, and changes in blood flow are often accompanied by comparable changes in glucose metabolism[4,5]. Accordingly, the BOLD amplitude acts as a proxy for metabolic energy demands and therefore carries direct physiological significance[4].

A central obstacle to interpreting regional BOLD amplitudes, however, is time. Neural processes unfold on diverse and time-varying timescales[6]. Fast unimodal fluctuations are integrated more slowly in transmodal networks[6], and neurovascular coupling adds additional lags and distortions[6,7]. As a result, two regions that engage in the same underlying operation may appear misaligned in time, which can obscure meaningful differences in signal amplitude, sometimes expressed in terms of signal energy or power. Common signal energy metrics, such as the amplitude of low-frequency fluctuations (ALFF)[8], fractional ALFF[9], and dynamic ALFF[10] capture amplitude but ignore temporal deformations; thus, genuine energy differences may be obscured when signals are misaligned in time. Conversely, dynamic connectivity methods— sliding window Pearson correlation[11], Hidden Markov models[12], phase synchronization[13], wavelet coherence[14], and lagged cross-correlation[15]— are largely amplitude-scale invariant by design, prioritizing synchrony over amplitude. As a result, both families can under-report signal-energy disparities in the presence of heterogeneous and time-varying processing rates. Contemporary deep-learning approaches[16-18] improve pattern capture but typically do not enforce an explicit alignment model for variable lags, leaving the core timescale problem unsolved.

We address this gap by advancing a systems principle of timescale normalization for coordinated signal-energy balance. The principle posits that, in health, the brain reconciles heterogeneous internal clocks so that inter-regional activity remains energetically proportionate over time. To operationalize this idea, we time-align regional BOLD signals with dynamic time warping (DTW), removing temporal distortions, and we develop a time-resolved DTW (trDTW) distance that isolates moment-to-moment amplitude differences. The resulting residual amplitudes over time define a dynamic signal-energy disparity between region pairs, quantifying inter-regional signal-energy imbalance and its heterogeneity. Importantly, these amplitudes and disparities are relative: preprocessing steps such as z-scoring remove mean and variance, placing values on an arbitrary, unitless scale. Thus, the dynamic signal-energy disparity yields a relative disparity measure rather than an absolute one.

Dynamic time warping aligns two signals by allowing small, relative local stretches and compressions of the time axis under continuity and monotonicity constraints, yielding an alignment cost that reflects dissimilarity despite variable delays and rates[19]. In fMRI studies, DTW has shown greater sensitivity to motor function, increased robustness to noise, superior test-retest reliability, and reduced dependence on global signal regression compared with correlation[20,21], and it detects group differences, including sex effects and diagnoses such as schizophrenia and autism[20-22]. Building on this literature, we introduced a warp elasticity metric that utilizes the DTW alignment path to quantify relative BOLD pacing (local time dilations/contractions) between networks[23,24], underscoring DTW's value in neuroimaging.

Grounded in DTW's established utility in fMRI, our time-resolved DTW leverages this foundation to yield a dynamic measure of inter-regional signal-energy disparity that remains robust to temporal misalignment. This framing leads to testable predictions. First, if timescale normalization supports coordinated signal-energy balance, healthy adults should show relatively homogeneous disparities across networks, whereas schizophrenia should show greater heterogeneity. Second, if balance is actively regulated, schizophrenia should show a slower return to a balanced signal-energy configuration after deviations. Third, because short-timescale processes challenge normalization most strongly, group differences should be most evident during faster fluctuations.

We first use simulations and phase-randomized surrogates to show that the measure reliably isolates amplitude-based disparities while tolerating timing variability. We then assess robustness with test-retest analyses in an independent healthy cohort (n = 1,200) across multiple sessions. Finally, we apply the framework to a multi-site schizophrenia cohort (controls =160, schizophrenia =151) to test whether heterogeneous signal-energy disparities and their Markovian state dynamics, particularly whether a slower return to a balanced signal-energy configuration, relate to symptom burden and cognition.

By centering timescale normalization and dynamic signal-energy balance as the organizing mechanism, this study provides a unifying account in which temporal variability is disentangled from amplitude, and disruptions of this balance may underlie clinically relevant dysregulation in schizophrenia.

2. RESULTS

2.1. Simulation of DTW sensitivity to non-stationarity and signal bandwidth

We evaluated DTW as a potential measure of inter-regional signal-energy disparity between brain networks through simulations assessing its ability to detect amplitude disparities and its invariance to phase shifts. Sinusoids with varying amplitude and phase modulations were generated, and we compared DTW to correlation. For DTW, we report both the standard DTW distance and a normalized DTW (nDTW), defined as the DTW

distance scaled by the alignment-path length, which yields values that are comparable across region pairs and, empirically, shows higher sensitivity to group differences[22]. We compared methods across DTW γ parameters and signal bandwidths (Supplementary Material).

DTW aligned original and temporally warped signals, demonstrating its capability to capture temporal deformations (Fig. 1a). Both DTW and nDTW remained invariant to non-stationary phase perturbations across increasing modulation indexes. In contrast, correlation decreased with higher phase modulation (Fig. 1b). In contrast, under non-stationary amplitude perturbations, correlation remained stable, while DTW and nDTW detected increasing amplitude disparities as modulation indexes rose (Fig. 1b).

The sensitivity of DTW and nDTW to amplitude scales was further examined by varying the γ parameter. Simulations involving amplitude non-stationarity across several modulation indexes revealed that smaller γ values resulted in higher rates of change in DTW and nDTW similarity scores at lower modulation indexes, indicating enhanced detection of minor amplitude disparities (Fig. 1c). Conversely, larger γ values exhibited higher rates of change at higher modulation indexes, reflecting improved tracking of substantial amplitude disparities (Fig. 1c). Additionally, while DTW generally maintains phase invariance, nDTW demonstrated slight sensitivity to phase differences when $\gamma \geq 1$ (Fig. 1c). This suggests that nDTW is better capable of responding to phase variations alongside amplitude tracking, offering a more nuanced assessment when absolute phase invariance is not essential.

In bandwidth analyses, DTW and nDTW sensitivity to randomness increased with broader full frequency spectrum, approaching the Nyquist frequency, unlike correlation, which remained unaffected (Fig. 1d). This indicates that amplitude differences become more prominent in broader full frequency bands.

Figure 1e illustrates nDTW ($\gamma = 1$) in capturing average aligned amplitude differences between brain networks. Lower nDTW values indicate convergence, reflecting more proportionate signal energy between regions, while higher values signify divergence, indicating greater signal-energy disparity between networks (Fig. 1e).

Fig. 1: Simulation to analyze non-stationarity and signal bandwidth

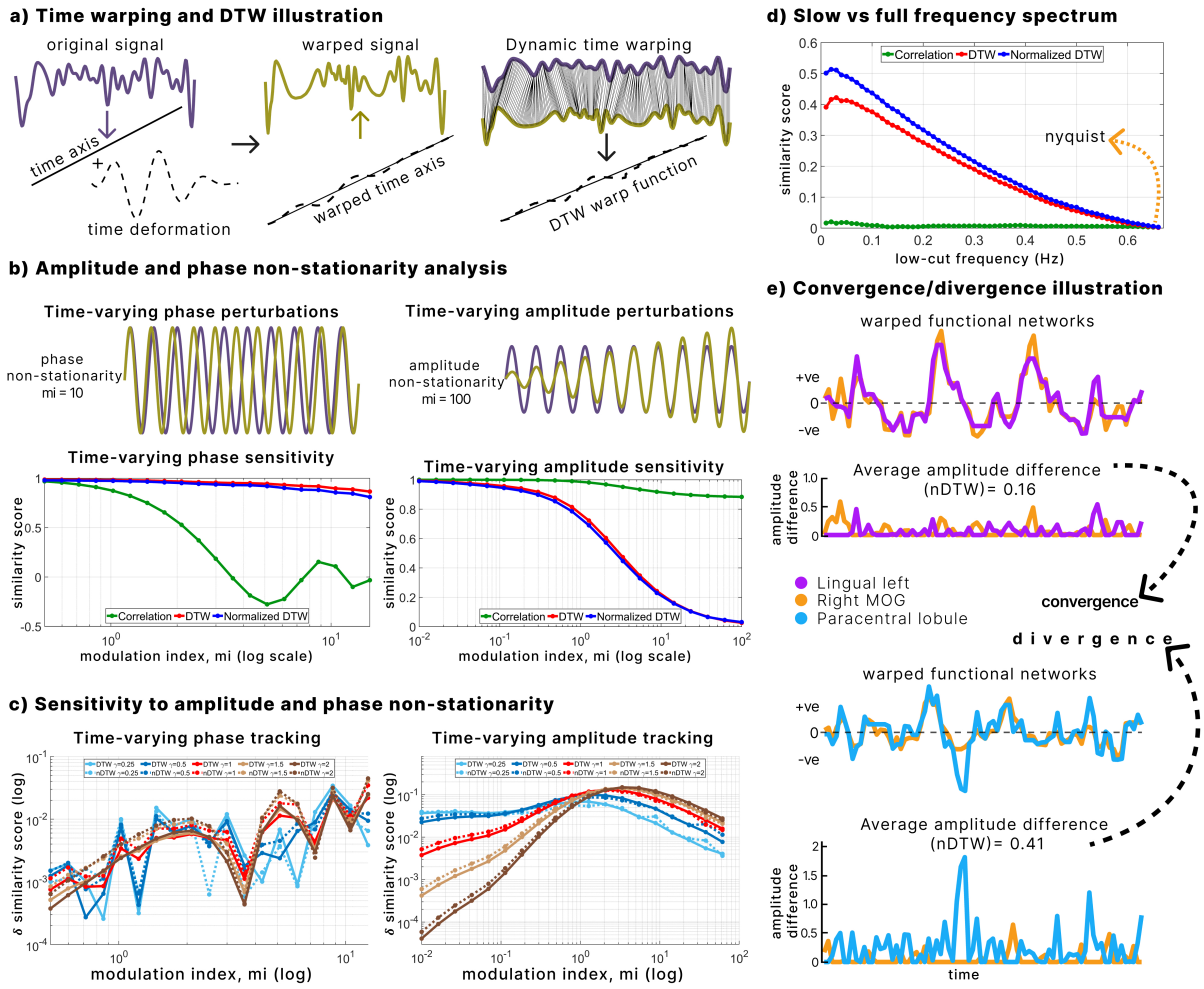

a. Illustration of DTW's ability to extract temporal deformations. A signal is warped by applying a modulation function (warp function) to its time index, and DTW successfully aligns the original and warped signals, extracting the induced temporal deformation. **b.** Behavior of DTW, nDTW and correlation under amplitude and phase non-stationarity. Time-varying amplitude perturbations (mi=100) and phase perturbations (mi=10) are shown. Similarity scores are derived from DTW and nDTW to highlight high distances (approaching 0) and low distances (approaching 1). Correlation is used as a benchmark. DTW and nDTW tracks amplitude disparities but remains invariant to phase shifts, unlike correlation. Both DTW and nDTW track amplitude disparities as mi increases (Time-varying amplitude sensitivity) but remain invariant to phase shifts, unlike correlation (Time-varying phase sensitivity). **c.** Sensitivity of DTW and nDTW to γ values in amplitude and phase non-stationarity. The derivative of similarity scores under amplitude non-stationarity reveals that for lower mi, smaller γ values yield higher scores compared to larger γ values, whereas for higher *mi*, larger γ values yield higher scores (Time-varying amplitude tracking). This indicates that smaller γ values are more adept at tracking minor amplitude disparities, while larger γ values are more suited to tracking larger amplitude disparities. Although DTW is inherently phase-invariant, nDTW exhibits slightly higher derivatives, indication slight sensitivity to phase differences when $\gamma \geq 1$ (Time-varying phase tracking). **d.** DTW sensitivity across signal bandwidths. Random signal pairs (i.i.d Gaussian, $\mathcal{N}(0,1)$) are filtered with increasing bandwidths up to the Nyquist frequency. DTW alignment and distances demonstrate increasing sensitivity to disparities in broadband signals, unlike correlation, which remains unaffected by the increasing frequency spectrum. This highlights DTW's suitability for capturing disparities in full spectrum signals against slow narrowband ones. **e.** Illustration of convergence and divergence in brain networks. Using nDTW with $\gamma = 1$, the average amplitude difference between two pairs of aligned brain networks is shown. A small nDTW indicates convergence, while a large nDTW signifies divergence in signal energy differences, providing insights into imbalances in signal-energy dynamics.

2.2. Inter-regional signal-energy disparities between schizophrenia and controls across broader fMRI bandwidths using nDTW

The intrinsic brain networks identified using the NeuroMark pipeline were categorized into seven domains: subcortical (SC), auditory (Aud), sensory motor (SM), visual (Vis), cognitive control (CC), default mode (DM), and cerebellum (Cb).

To validate nDTW in the context of faster BOLD fluctuations, we extended our analysis to include broader frequency bands (slow-5, slow-4, and slow-3; 0.01–0.198 Hz). We also examined the impact of varying γ values on test–retest reliability and sensitivity to group differences.

Focusing on the broader band (0.01–0.198 Hz; hereafter F1), we observed that test–retest reliability improved with higher γ values, as indicated by lower mean ranks (Fig. 2a). γ values of ≥1.5 demonstrated significantly higher reliability compared to correlation after false discovery rate (FDR) (Wilcoxon signed-rank test, FDR corrected $p < 0.05$). Given that physiological noise correction in the fMRI data reduces within-subject variability[25], thus increasing test-retest reliability, the higher test-retest score for higher γ values may be indicative of the reduced sensitivity of higher γ values to physiological noise in the data.

Figure 2b illustrates that γ values of 1.5 and 1.25 exhibit the highest sensitivity for detecting group differences across both frequency ranges, outperforming other γ values and correlation. These γ values outperform other parameters and the correlation benchmark, as indicated by the greater number of directional arrows pointing towards them and the significant sensitivity enhancements marked by yellow asterisks. However, since $\gamma = 1.25$ has significantly lower test–retest reliability than the correlation benchmark (Fig. 2a), $\gamma = 1.5$ was selected as the optimal parameter for further analysis. Additionally, nDTW consistently detected more group differences in the broader F1 frequency range than in F2 across all γ values, whereas correlation did not. This indicates that nDTW is more sensitive to detecting clinically relevant group differences during faster BOLD fluctuations while maintaining high test–retest reliability, particularly at $\gamma = 1.5$.

Figure 2c shows that controls (lower triangle) consistently exhibit lower signal-energy disparity (greater convergence), whereas individuals with schizophrenia (upper triangle) display greater signal-energy disparity (greater divergence) across several brain network pairs. This suggests that controls maintain more proportionate signal energy between networks, whereas schizophrenia shows greater imbalance. Controls displayed significantly more convergence (lower signal-energy disparity) than individuals with schizophrenia across multiple brain-network pairs (positive red cells in the upper triangle of the FDR-corrected group-difference matrix; Fig. 2c). Additionally, Cohen's d effect

sizes (min-max = $0.19 - 0.89$; median = 0.49) highlight the practical significance of these group differences.

Furthermore, significant associations between signal-energy disparity (nDTW) and PANSS scores were identified. Higher positive PANSS scores were primarily associated with greater signal-energy disparity between Cb networks and the DM, CC, and superior temporal gyrus (Aud), as well as Vis and SC networks. Higher negative PANSS scores were mainly associated with greater signal-energy disparity between CC, DM, and Vis networks.

Fig. 2: Reliability and group difference sensitivity across γ values and frequency bands

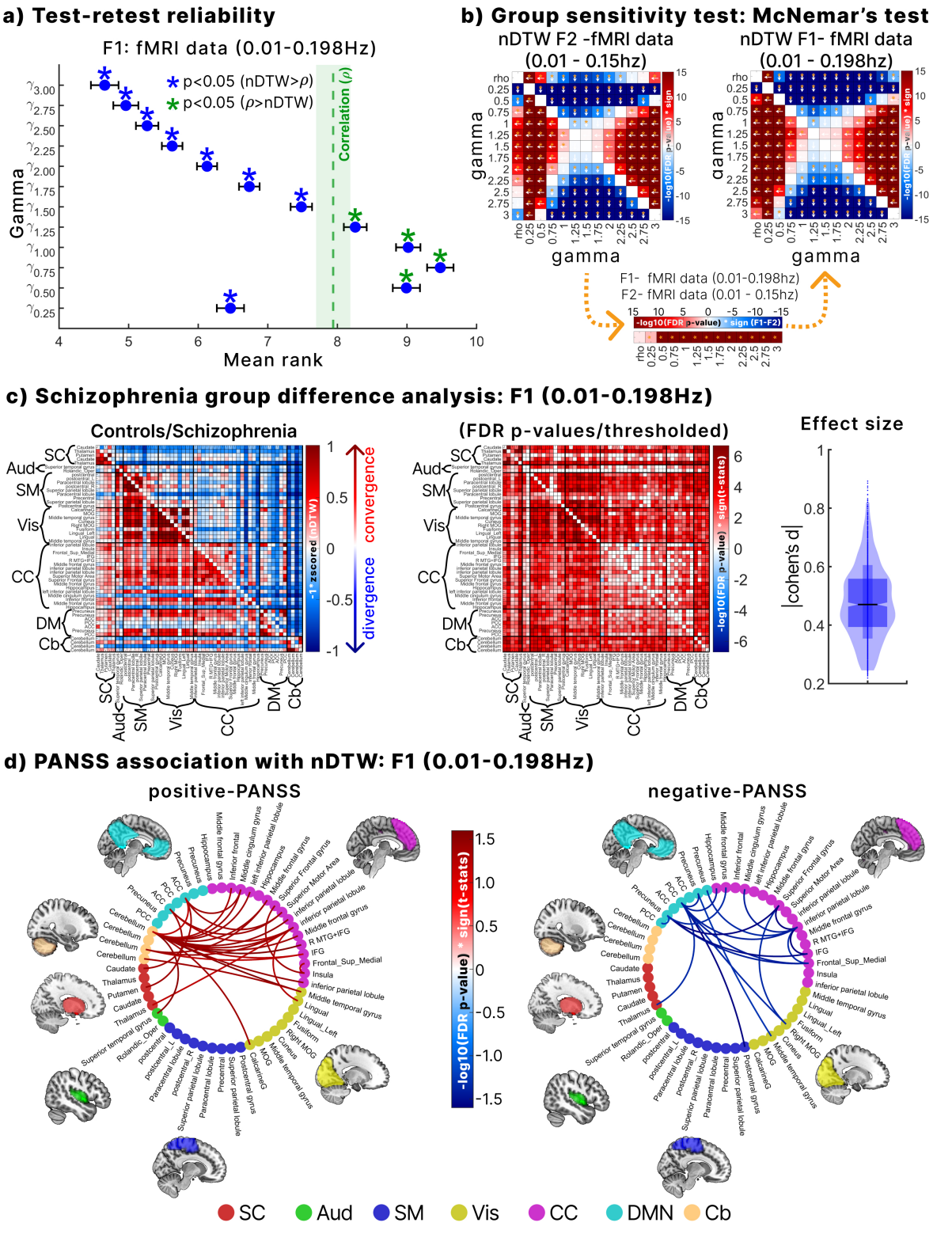

a. Test-retest reliability of nDTW was evaluated across multiple γ values using the HCP dataset, with correlation serving as a benchmark. The mean ranks for all twelve γ values and correlation are presented for the F1 frequency range. Lower mean rank values indicate higher test-retest reliability. γ values ≥ 1.5 and $\gamma = 0.25$ show significantly higher test-retest than correlation, as determined by a Wilcoxon signed-rank test (FDR-corrected $p < 0.05$) on the test–retest ranks. **b.** Gamma sensitivity in distinguishing schizophrenia from controls. We applied McNemar tests across all γ values for the F1 and F2 frequency ranges, as well as between F1 and F2. In the resulting matrices, arrows point to the parameter with higher sensitivity, and yellow asterisks highlight significant results with FDR-corrected p-values < 0.05. Results showed that γ values of 1.5 and 1.25 are the most effective in distinguishing schizophrenia patients from controls compared to other γ values and correlation for both F1 and F2 frequency ranges. Furthermore, the comparison between F1 and F2 demonstrates that all γ values increase group difference sensitivity when transitioning from F1 to F2, whereas correlation (rho) does not. These findings suggest that nDTW is more sensitive to group differences when higher frequencies are incorporated. **c.** Group difference between schizophrenia and controls using a $\gamma = 1.5$. nDTW values were z-scored across both groups and multiplied by -1, converting smaller nDTW values to positive scores (indicating convergence) and larger values to negative scores (indicating divergence). Group averages of nDTW scores reveal that controls exhibit convergence (lower triangle) while individuals with schizophrenia show divergence (upper triangle) across several brain network pairs. FDR-corrected p-values from a generalized linear model, controlling for sex, age, site, and mean frame displacement, are displayed in the lower triangle, with significant results (FDR < 0.05) highlighted in the upper triangle. The findings indicate that multiple brain network pairs show significant differences, with controls consistently demonstrating greater convergence than schizophrenia patients. Additionally, Cohen's d effect sizes exceeding 0.2 underscore the practical relevance of these group differences. **d** Association of nDTW with PANSS scores. Significant associations between brain network pairs and both positive and negative PANSS scores (FDR-corrected $p < 0.05$) were identified using a generalized linear model with a Poisson distribution. The analysis controlled for sex, age, site, and mean frame displacement. These significant associations are displayed for both positive and negative PANSS, highlighting the relationship between nDTW scores and symptom severity in schizophrenia.

2.3. Effects of including faster BOLD fluctuations on signal-energy disparity

We evaluated the effect of nDTW on expanding the frequency range from F2 to F1 by conducting paired sample t-tests for controls and individuals with schizophrenia separately. Normality of nDTW scores was confirmed using Shapiro-Wilk tests with t-values close to 1 across brain network pairs (Fig. 3a). After FDR correction, controls exhibited significantly lower signal-energy disparity (greater convergence) in F1 compared to F2, whereas individuals with schizophrenia showed higher signal-energy disparity (greater divergence) in F1 versus F2 across specific brain network pairs. These results suggest that including the broader band (F1) supports more proportionate signal energy in controls but amplifies imbalance in schizophrenia, indicating that including faster BOLD fluctuations increases sensitivity to group differences.

Cohen's d effect sizes were modest (median $d = 0.18$ for controls and $d = 0.15$ for schizophrenia). Nonetheless, higher frequencies amplified group distinctions, as reflected by larger effect size differences between controls and schizophrenia across several brain network pairs (Fig. 3a). Upset plot analysis identified 914 significant pairs across both frequencies, with 196 unique to F1 and 10 unique to F2, highlighting the enhanced group sensitivity of nDTW in F1 (Fig. 3b).

Figure 3b displays FDR-corrected p-values for significant pairs shared by both frequencies (left panel), with F1 (lower triangle) showing higher practical relevance than F2 (upper triangle) based on effect sizes. Pairs unique to F1 had Cohen's $d > 0.2$, underscoring nDTW's increased sensitivity to clinically relevant group differences when faster fluctuations are included.

To validate F1-unique pairs, we conducted null hypothesis testing using 1,000 surrogate datasets generated through phase randomization within the 0.15–0.198 Hz range (Fig. 3c). Several network pairs remained significant, confirming that effects involving faster fluctuations are statistically robust and potentially derived from non-stationary amplitude processes.

Finally, we examined PANSS associations observed in F1 but not F2. Positive PANSS correlated with connections between the Cb with SC, DM, CC, Aud, and Vis networks. Negative PANSS was primarily associated with CC-DM connections. These associations were absent in F2, suggesting that including faster BOLD fluctuations improves sensitivity to symptom associations.

Fig. 3: Clinical significance of high frequency fMRI data inclusion.

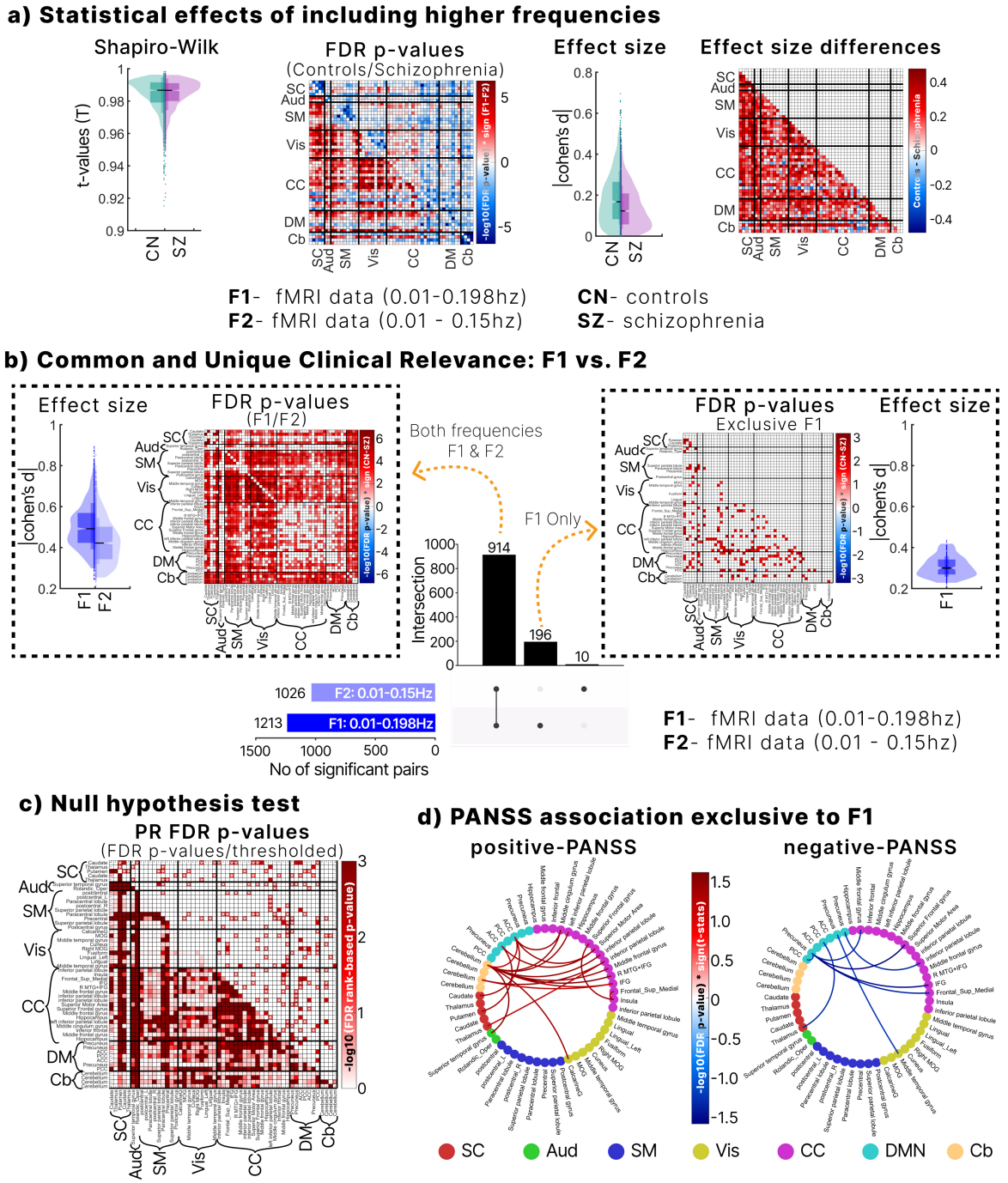

a. Statistical analysis of signal-energy imbalances between F1 and F2 frequencies. Shapiro-Wilk tests confirmed normality ($T\text{-}values \approx 1$) for all groups, validating the use of paired t-tests. FDR-corrected p-values of paired t-test indicated that controls exhibit increased signal energy convergence, whereas individuals with schizophrenia show signal-energy divergence when transitioning from F2 to F1. This suggests that controls demonstrate greater convergence, while schizophrenia patients exhibit increased divergence with the inclusion of higher frequencies. Cohen's d effect sizes (~0.4) highlight enhanced separability between groups. **b.** Group differences from a generalized linear model controlling for sex, age, mean frame displacement, and site. FDR-corrected p-values across brain network pairs revealed 914 common significant pairs, with F1 showing larger effect sizes and greater practical relevance (left panel). Additionally, 196 significant pairs were uniquely identified in F1 with effect sizes above 0.2 (right panel), indicating modest practical relevance, while only 10 pairs were unique to F2. **c.** Null hypothesis testing using phase randomization confirmed that the significant brain network pairs uniquely identified in F1 are statistically relevant. **d.** Associations between normalized nDTW and PANSS scores were exclusively observed in the F1 frequency range, with no significant associations found in F2.

2.4. Dynamics of time-resolved DTW

To identify recurring states of signal-energy imbalance dynamics, we applied k-means clustering with three clusters on the time-resolved DTW, including both controls and individuals with schizophrenia. An elbow plot (Fig. 4c) confirmed that three clusters were optimal, determined by the derivative of the within-sum of squared distances. For visualization, we subtracted the median of all clusters and multiplied the distribution by -1, ensuring positive values represent convergence and negative values indicate divergence (Fig. 4a). The clusters were classified as follows: state 1—a convergent state, state 3—a divergent state, and state 2—a mixed state showing neither strong convergence nor divergence.

Figure 4b illustrates brain network representations for each state. In convergent state 1, the top 5% most convergent pairs predominantly involved sensory networks, including Vis, SM, and Aud networks. The divergent state 3 featured the top 5% most divergent pairs, mainly between the Cb and other networks. The mixed state 2 showed the top 2.5% most convergent and top 2.5% most divergent pairs, combining both dynamics.

A Markov chain was constructed to model state transitions, with transition probabilities shown in Figure 4d. Mixed state 2 had the highest self-retention probability (0.9021), followed by the convergent state 1 (0.8485) and divergent state 3 (0.8133). No direct transitions occurred between divergent and convergent states, consistent with a regime in which shifts proceed through an intermediate mixed state.

The Markov chain's "stable point" (stationary distribution: Fig. 4e) showed that mixed state 2 accounted for 57.36% of system dynamics, the convergent state 1 for 37.21%, and the divergent state 3 for 5.42%. This highlights the predominance of mixed and convergent states in stabilizing signal-energy balance dynamics.

We further analyzed these dynamics by calculating the entropy rate and the rate of return to the stationary distribution (spectral gap). The entropy rate was 36.6%, where 100%

represents complete randomness and 0% indicates full order. This suggests a balance between randomness and order, with a slight preference for order (Fig. 4f). The rate of return (spectral gap) was 0.1851, and the mixing time—defined as the number of timesteps required to reach a tolerance level of 10^{-3} from the stationary distribution—was 36 timesteps (72 seconds; TR=2). The mixing time was determined from the farthest distribution point in the Markov chain's state space, specifically the state [0, 0, 1] (completely divergent), as shown in Fig. 4e.

We explored the relationship between entropy and convergence rate and ran an exploratory perturbation analysis to assess how modifying transition probabilities would affect the rate of return and entropy (Fig. 4g–h). Increasing self-retention in any brain state led to reductions in both convergence rate and entropy rate. While adding transitions between the mixed state and other states (excluding mixed to divergent) enhanced both rates, transitions between divergent and convergent states were marked with red crosses due to their impracticality, as no such transitions were identified in the dynamics (Fig. 4d).

Notably, increasing transition probability from mixed to divergent states extends trajectories away from the stable point (Fig. 4e), slowing the return to the stationary distribution. While this increased entropy, our findings suggest that higher entropy does not universally speed the return to stationarity; instead, the effect depends on the specific dynamic transitions within the Markov chain's state space.

Fig. 4: Dynamics of time-resolved DTW

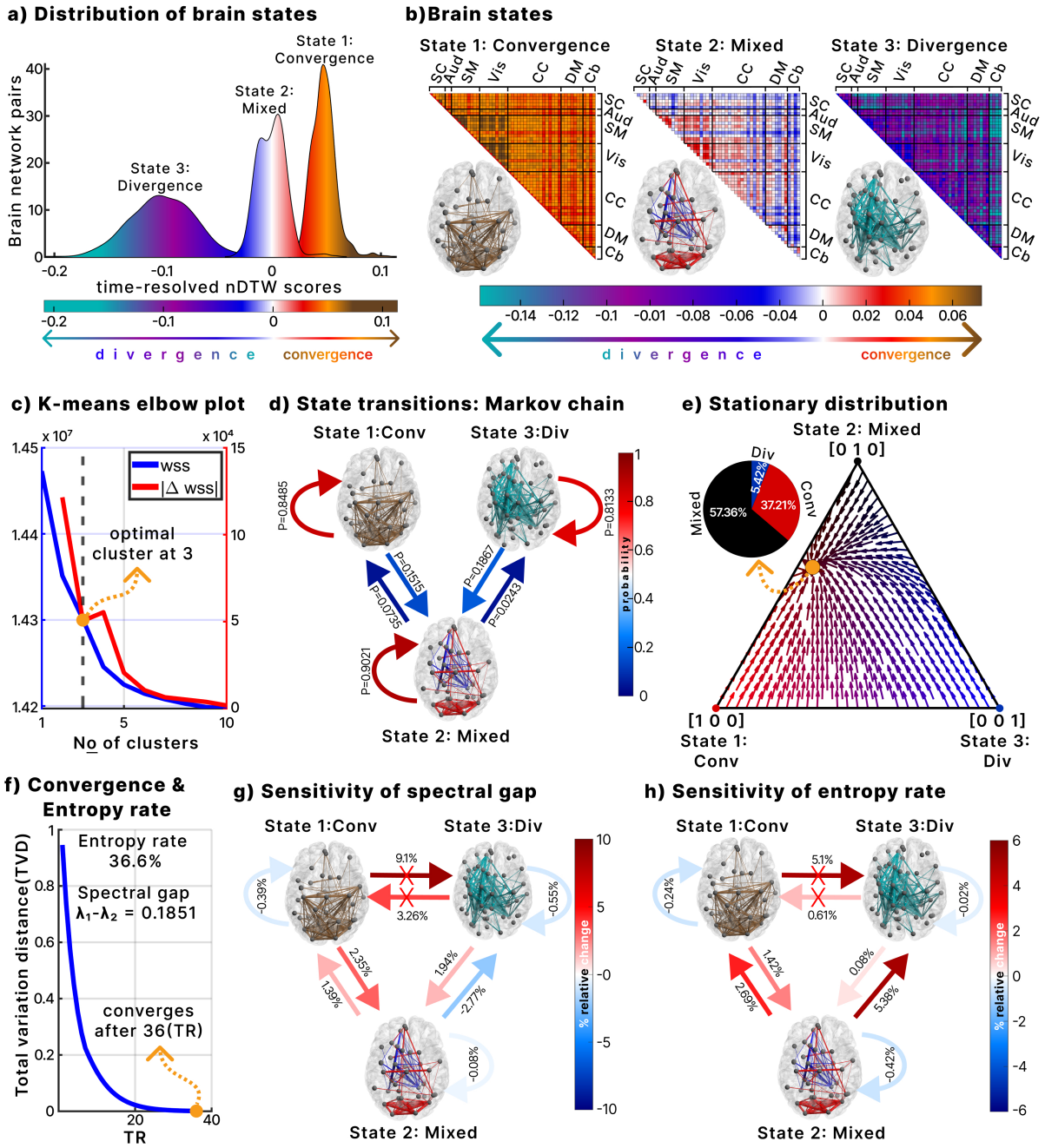

266

a. Distribution of recurring brain states identified using K-means clustering on time-resolved DTW. The median across all 3 cluster centroids were subtracted and multiplied by –1 to ensure positive values represent convergence and negative values represent divergence. Three states were identified: convergent, divergent, and mixed. **b.** Brain state matrices with corresponding axial brain thumbnails. For convergent and divergent states, the top 5% most convergent and 5% most divergent brain connections are displayed, respectively. The mixed state shows the top 2.5% most convergent and top 2.5% most divergent connections. **c.** Elbow plot illustrating the within-sum of squared distances (WSS) for different cluster numbers. The first inflection point in the first derivative of WSS indicates that three clusters are optimal. **d.** State transition probabilities between the identified brain states, highlighting the likelihood of moving from one state to another. **e.** Stationary distribution within the Markov chain state space, demonstrating that the stable point of the dynamics is predominantly influenced by the mixed and convergent states. **f.** Mixing time of the dynamics, indicating the number of timesteps required to converge to the stationary distribution within a tolerance of 10^{-3}. Additionally, the convergence rate is shown through the spectral gap and entropy rate. **g.** Effects of perturbing state transitions on the spectral gap. Small perturbations were added to each transition probability, and the relative change in spectral gap was calculated to assess changes in convergence rate. **h.** Effects of perturbing state transitions on the entropy rate.

2.5. Group differences between controls and schizophrenia

We assessed group differences in metrics derived from time-resolved DTW, including mean dwell time, occupancy rate, state transition probabilities, stationary distribution, spectral gap, mixing time, and entropy rate. Schizophrenia patients showed a greater association with mixed state 2 and divergent state 3, while controls predominantly engaged with the convergent state 1. Specifically, schizophrenia patients had longer mean dwell times in mixed and divergent states, whereas controls spent more time in the convergent state (Fig. 5a). Similarly, occupancy rates (Fig. 5b) reflected higher mixed and divergent state occupancy in schizophrenia, and greater convergent state occupancy in controls.

The stationary distribution (Fig. 5d) revealed that schizophrenia dynamics are more influenced by mixed and divergent states than controls, while controls are more influenced by the convergent state than schizophrenia. State transition probabilities showed controls were more likely to transition from mixed to convergent states (Fig. 5c). In contrast, schizophrenia patients had increased transitions from convergent to mixed, mixed to divergent, and higher self-retention in both mixed and divergent states.

Fig. 5: Group differences and cognitive score associations

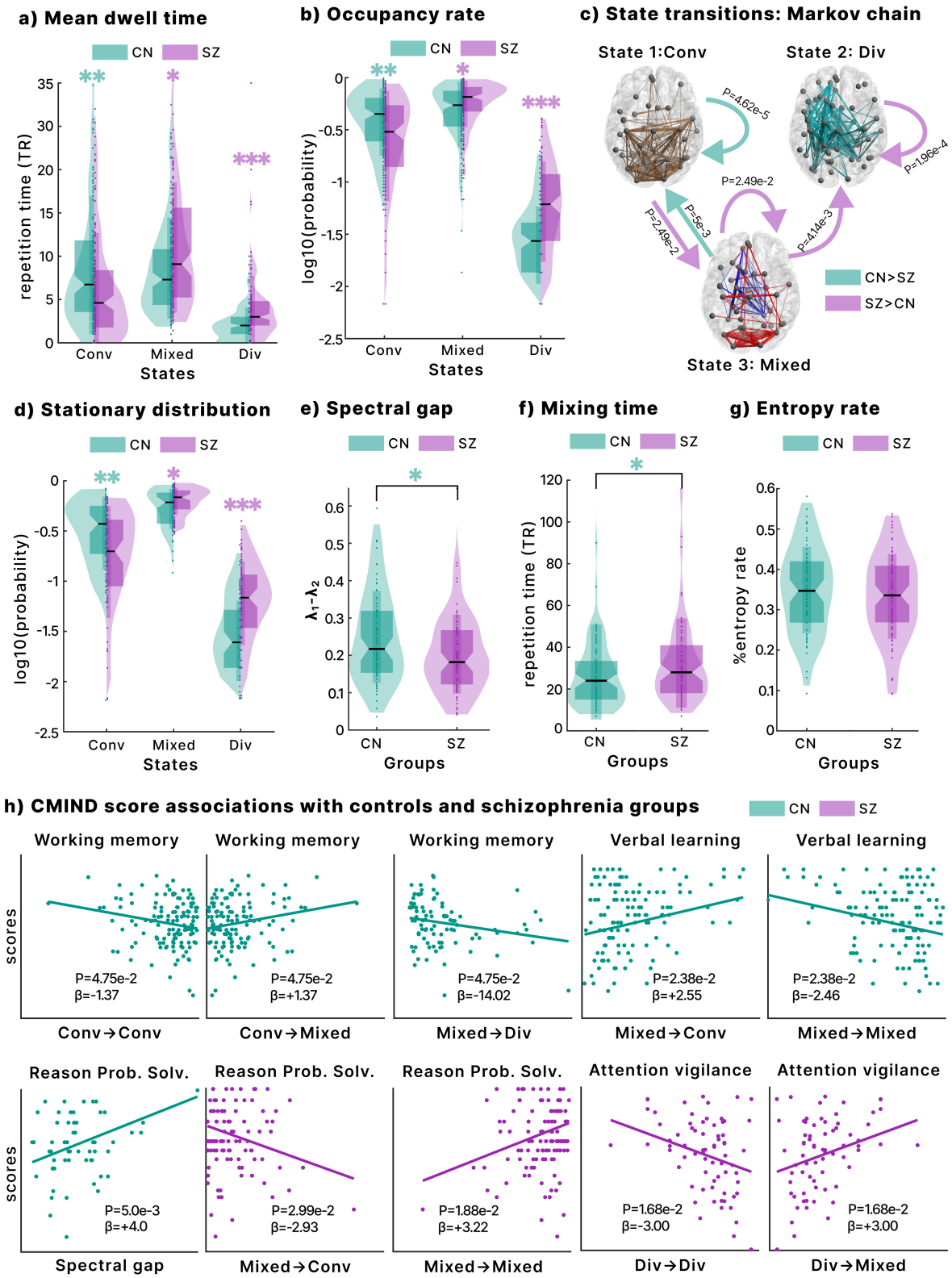

285

a. Mean dwell time in each state for schizophrenia patients and controls, highlighting increased dwell time in mixed and divergent states for schizophrenia and convergent state for controls**. b.** Occupancy rate of each state, showing longer occupancy in mixed and divergent states for schizophrenia and in convergent state for controls. **c.** State transition probabilities between states for schizophrenia patients and controls, illustrating higher transition rates from convergent to mixed and mixed to divergent states in schizophrenia. **d.** Group difference in stationary distribution of the Markov chain. **e.** Spectral gap, reflecting the convergence rate, is higher in controls compared to schizophrenia patients, suggesting faster convergence to the stable point in controls. **f.** Mixing time, representing the number of timesteps required to reach the stationary distribution within a tolerance of 10^{-3}, is shorter in controls than in schizophrenia patients, indicating quicker convergence in controls. **g**. Entropy rate, showing the balance between order and flexibility, does not differ significantly between groups. **h.** Associations between cognitive scores and nDTW metrics, analyzed separately for each group to account for group bias. In controls, working memory and verbal learning are associated with specific state transitions and spectral gap is associated with reasoning and problem-solving. In schizophrenia, reasoning, problem-solving, and attention vigilance are linked to different transitions and state retention.

All analyses were conducted using generalized linear models controlling for sex, age, site, and mean frame displacement. Results were FDR-corrected with a significance threshold of 0.05. One asterisk (*) indicates p-values between 0.05 and 0.01, two asterisks (**) indicate p-values between 0.01 and 0.001, and three asterisks (***) indicate p-values below 0.001.

Regarding return to the stationary distribution, controls exhibited a higher spectral gap, indicating a faster rate of return (Fig. 5e). Using a tolerance of 10^{-3} and starting from the completely divergent state ([0, 0, 1]), controls also had a lower mixing time, reflecting a faster return to a “stable” signal-energy configuration. No significant difference in entropy rate was observed, suggesting that the faster rate of return in controls may reflect differences in transition structure rather than entropy.

2.6. Associations with cognition in controls and schizophrenia

We examined associations between time-resolved DTW metrics and Computerized Multiphasic Interactive Neurocognitive System (CMINDS) scores using generalized linear models (GLM) for controls and schizophrenia patients separately to avoid group bias (Fig. 5h).

In controls, working memory was positively associated with transitions from convergent to mixed states and negatively associated with convergent self-retention and mixed-to-divergent transitions, indicating that transitions into the mixed state support memory performance. Verbal learning was positively associated with transitions from mixed to convergent states and negatively with convergent-to-mixed transitions, suggesting that the convergent state facilitates verbal learning. Additionally, the spectral gap was positively associated with reasoning and problem-solving, highlighting the link between faster convergence rates and higher cognitive performance.

In schizophrenia, reasoning and problem-solving were negatively associated with transitions from mixed to convergent states but positively with self-retention in the mixed state. Attention vigilance was positively associated with transitions from divergent to mixed states and negatively with self-retention in the divergent state. These results

indicate that specific dynamic transitions were differentially associated with cognitive performance in schizophrenia; for example, moving into the mixed state was related to better attention vigilance, whereas remaining in the divergent state was related to poorer attention.

3. DISCUSSION

This study developed a comprehensive framework to assess signal-energy imbalances between brain networks using fMRI data, providing a timing-invariant readout of amplitude differences while accounting for varying temporal scales of brain activity. The physiological basis of the BOLD signal amplitude is not entirely straightforward. Studies combining fMRI with PET imaging have shown that the amplitude of the BOLD signal can track glucose utilization in the brain[4,5]. However, studies show that even when blood and oxygen are already abundant (hyperemia and hyperoxia), neuronal activation still elicits a BOLD increase. This suggests the BOLD signal amplitude does not simply reflect shortage of glucose or oxygen[26,27]. Research further supports this by proposing that, due to the slow response of the neurovascular coupling, neurons initially rely on astrocytic glycogen and lactate stores before blood flow compensates for energy use[28,29]. This indicates that blood flow does not simply match real-time neuronal energy consumption[30]. Nevertheless, neuronal activation consistently triggers vasoactive signaling, leading to vasodilation through neurovascular coupling, regardless of brain baseline oxygen or glucose levels[27]. In this sense, while the *immediate* energy source may vary, BOLD amplitude can be interpreted as a proxy for overall energy *demand*, whether supplied by circulating glucose/oxygen or intracellular reserves. Building on this relevance of BOLD amplitude, our DTW-based approach quantifies relative inter-regional amplitude differences, providing a timing-invariant measure of signal-energy disparity that remains robust to temporal variability from both neural processing and hemodynamic modulation.

By utilizing our recently proposed nDTW metric[22], we explored functional relevance beyond the typical 0.01–0.15 Hz range. Our time-resolved DTW identified three intuitive brain states: convergence (lower signal-energy disparity)**,** divergence (higher signal-energy disparity)**,** and a mixed state, indicating flexibility in signal-energy balance. Simulations confirmed the robustness of nDTW in capturing aligned amplitude disparities between signals, tracking non-stationary amplitude changes, and remaining invariant to timing and phase deformations. Importantly, our framework demonstrated functional relevance by associating state dynamics of signal-energy disparity with clinical and cognitive scores.

Static results revealed that control subjects exhibited stronger convergence, while schizophrenia showed relatively greater divergence in inter-regional signal-energy

disparities. Our static analysis suggests that healthy controls maintain more proportionate signal energy across brain networks globally, whereas individuals with schizophrenia exhibit significant imbalances. These observations are consistent with prior reports of altered physiological and metabolic processes in schizophrenia[31,32], without requiring a direct metabolic inference from our measure.

A key finding was the increased convergence in controls and increased divergence in schizophrenia when the broader band, including faster BOLD fluctuations, was included. These results indicate that including faster BOLD fluctuations improves sensitivity to group differences. In controls, the inclusion of these frequencies was associated with more proportionate signal energy across brain networks, while in schizophrenia, it was associated with greater imbalance. Furthermore, several brain network pairs showed significant differences between controls and schizophrenia exclusively when faster BOLD fluctuations were included. The phase-randomized null model confirmed that these results were statistically significant and likely attributable to non-stationary amplitude processes detected by nDTW. While synchronization studies have established the functional relevance of faster BOLD fluctuations[33], our findings provide a novel perspective. We demonstrate that including faster BOLD fluctuations improves the distinction between control individuals and those with schizophrenia by capturing non-stationary aligned-amplitude disparity during rapid neural processing.

We also found positive associations between nDTW and positive symptoms, particularly in connections involving the cerebellum with the Aud, DM, CC, SC, and Vis domains. The cerebellum, recognized as a key predictive hub in the brain[34], not only regulates rapid cognitive processing—including speed, capacity, and consistency[35]— but also plays a central role in orchestrating mental coordination. This observation aligns with the "cognitive dysmetria" theory, which attributes schizophrenia to impaired coordination among prefrontal regions, thalamic nuclei, and the cerebellum[36].

Our findings further support this theory, revealing that altered cerebellar coordination of neural processing is linked with positive symptoms[36]. Specifically, lower divergence, or relatively higher convergence, in schizophrenia was correlated with more severe positive symptoms such as hallucinations, delusions, and disorganized thinking. Considering that our results show significantly stronger convergence in controls compared to individuals with schizophrenia, the observed positive associations with symptom severity may indicate maladaptive or compensatory [37] cerebellar influences on signal-energy balance, inadvertently co-occurring with positive symptomatology in the affected networks.

Negative associations were observed between brain networks and negative symptoms, indicating that lower convergence (or higher divergence) is linked to more severe negative symptoms. These associations were most prominent between higher-order processing networks such as DM and CC. Given that negative symptoms, characterized by reduced

motivation, pleasure, and emotional expression, are linked to high-level cognitive processing[38], our findings suggest that greater signal-energy imbalance within and between the DM and CC is associated with increased negative symptoms in schizophrenia. Prior studies have connected impaired physiology and metabolism to negative symptoms like depression[39,40], and a recent study found that improvements in metabolic measures, achieved through prefrontal cortex stimulation, were associated with reductions in negative symptoms[41]. Our results complement this literature by providing a timing-invariant, amplitude-based fMRI marker that relates to symptom severity.

Notably, most of the PANSS associations identified were due to the inclusion of higher frequencies, emphasizing the importance of including faster BOLD fluctuations. Although higher frequency bands have been associated with various sources of noise[42], work has also identified high frequency fluctuations as a source of non-noise variability[33,43,44]. Alterations within such frequency bands may therefore reflect alterations to rapid neural processing in schizophrenia.

Our framework identified three dynamic states: convergent, divergent, and mixed. The convergent state reflects relatively lower inter-regional signal-energy disparity, suggesting that neural circuits are operating within a more proportionate amplitude regime. Conversely, the divergent state represents higher signal-energy disparity, where certain brain networks show larger aligned-amplitude differences. Such an imbalance may destabilize functional interactions, ultimately leading to reduced cognitive performance[40,45,46]. The mixed state lies between these extremes, reflecting neither strong convergence nor strong divergence. Transitions were observed only between the mixed and either the convergent or divergent states, with no direct shifts between convergent and divergent states (Fig. 4d). Thus, the mixed state appears to function as an adaptive intermediary, enabling the brain to switch flexibly between functional states as needed.

The brain criticality theory posits that the brain functions near a critical point, a delicate balance between order and disorder[47]. The mixed state in our framework is consistent with this balance, contributing 57.36% to the stationary distribution. Combined with the Markov chain's entropy rate of 36.6%, this finding suggests that the brain operates closer to the critical entropy point of 50% rather than being too ordered or too disordered, with a slight bias toward order that remains within the "zone of criticality"[48]. Indeed, critical entropy serves as an indicator of brain criticality[49], a state that helps the brain maintain flexibility and adaptability in its functions. We interpret these links cautiously as consistency rather than a direct test of criticality.

A key dynamic metric in our study is the rate of return to the stationary distribution (spectral gap), which measures how quickly a system reaches its stable state. Our

perturbation analysis revealed that increasing self-retention probabilities reduced both the rate of return and entropy rates. This is because higher self-retention enforces predictability, which runs counter to the flexibility required by criticality theory. Generally, higher rates of return correlated with increased entropy, except for transitions from the mixed to divergent state—highlighting the significant role of transition dynamics in return dynamics. State space analysis further demonstrated that trajectories moving from the divergent state take the longest to reach the stable point (Fig. 4e), thereby validating why increasing mixed to divergent transitions reduces the rate of return to the stable point. This pattern underscores the need to balance order and disorder (i.e., to increase entropy) while optimizing the trajectory toward stability.

Importantly, control subjects exhibited significantly higher rates of return, evidenced by metrics such as the spectral gap and mixing time, compared to patients with schizophrenia, despite both groups maintaining similar entropy levels. This suggests that although both groups operate near critical entropy, the dynamics of schizophrenia hinder efficient return to balance, likely due to altered transition pathways. These findings further imply that high entropy does not necessarily equate to enhanced information integration or superior cognitive performance, challenging the notion that richer conscious experiences always result from increased entropy[50].

Cognitive flexibility was further underscored by the associations observed with the mixed state. In control subjects, working memory performance was positively linked to transitions from convergent to mixed states and negatively associated with both self-retention in the convergent state and transitions from mixed to divergent states. These relationships suggest that the mixed state, reflecting flexible signal-energy balance dynamics, was associated with the flexibility necessary for effective higher-order functions such as working memory[51]. In individuals with schizophrenia, reasoning and problem-solving abilities were negatively associated with transitions from mixed to convergent states, while showing positive associations with self-retention in the mixed state and transitions from divergent to mixed states. Additionally, attention vigilance was negatively related to self-retention in the divergent state but positively correlated with transitions from divergent to mixed states. Overall, these findings emphasize the associational role of the mixed state in supporting cognitive flexibility and indicate that disruptions in transitions to and from this state may contribute to the cognitive impairments observed in schizophrenia.

However, the mixed state may not be optimal for every task. For example, in control subjects, transitions from the mixed to convergent state were positively associated with verbal learning, whereas extended self-retention in the mixed state showed negative associations. Given findings that verbal learning benefits from structured cognitive training[52], consistent with the ordered nature of the convergent state, it appears that while

the mixed state promotes flexibility, tasks that require structured cognition may rely more on the consistency of the convergent state. Overall, these results underscore the importance of balancing flexibility and stability to optimize cognitive performance.

Group-level analysis revealed that controls predominantly engaged in the convergent state, while schizophrenia subjects showed greater involvement in the mixed and divergent states. Metrics such as mean dwell time, fraction rate, state transitions and stationary distribution confirmed these patterns. The increased presence of divergent states in schizophrenia aligns with the disorder's characteristic disruption in neural dynamics[53]. Furthermore, as transitions toward the mixed state were found to decrease the rate of return to stability, the excessive engagement of the mixed state in schizophrenia may reflect an overly sustained flexibility that potentially undermines cognitive processes such as working memory.

Although this study offers a unifying framework across brain mechanisms, BOLD fMRI reflects relative rather than absolute energetic changes. Preprocessing through z-scoring removes mean and variance, and ICA adds further scale ambiguity by maximizing statistical independence on unitless signals. As a result, all amplitudes analyzed in this study, and the disparities derived from them, are on a relative scale that cannot be directly mapped onto absolute physiological energy demands. Nevertheless, relative fluctuations in ICA time courses remain informative about how brain networks differentially engage neural activity and its associated energetic requirements.

In summary**,** we provide evidence to suggest that schizophrenia is characterized by a pronounced inter-regional signal-energy disparity across the brain, both throughout the scanning session and dynamically, becoming more evident during rapid neural processing. Additionally, we observed greater signal-energy disparity in a hub-like interaction between the cerebellum and other brain networks linked to positive symptoms, while heightened disparity across high-order processing networks, such as the DM and CC, was associated with negative symptoms. Our findings provide a novel and intuitive perspective on brain criticality using time-aligned fMRI signals, revealing that cognitive flexibility, a key marker of brain criticality, is linked to improved working memory and fluid intelligence in both controls and individuals with schizophrenia. However, we also establish that cognitive flexibility may hinder performance on structured tasks like verbal learning. Furthermore, transitions into a state of greater signal-energy disparity are associated with declines in attention and vigilance in schizophrenia. Finally, we propose a therapeutic intervention in the Supplementary material using photobiomodulation and the developed directional DTW. This comprehensive framework linking time-aligned BOLD amplitude dynamics to cognition and schizophrenia symptoms offers a unifying perspective for various hypotheses of brain function in neuroscience research.

4. METHODS

4.1. Dynamic time warping as a measure of signal-energy disparity

Dynamic time warping is a widely used signal processing algorithm that aligns signals with nonlinear temporal deformations by applying adaptive "elastic" transformations to achieve a meaningful similarity measure[19,54]. When temporal deformations complicate phase or timing relationships, it becomes logical to isolate these aspects and concentrate solely on the amplitude of the signals. DTW tackles this by resolving temporal dissimilarities, optimally aligning signal pairs to minimize a distance metric and bring them to a shared temporal scale, leaving amplitude as the primary source of disparity.

The algorithm computes a distance cost matrix that captures the cumulative cost of aligning pairwise elements of the sequences and identifies the optimal warping function to adjust their time axes, minimizing a distance metric. To enhance computational efficiency and ensure meaningful alignments, particularly when guided by domain knowledge, a window size constraint is applied to limit the maximum allowable warping between indices in the time series[19].

For discrete signals x and y of lengths N and M respectively, the distance cost matrix, $CM_{DTW(i,j)}$, is initialized as follows:

$$CM_{DTW(i,j)\epsilon(x,y)} = \begin{cases} 0, if\ (i,j) = (0,0) \\ +\infty, otherwise \end{cases}$$

The cells in $CM_{DTW(i,j)}$ that are within the allowable window, w, can be defined as:

$$CM_{DTW(i_w,j_w)\epsilon\{|i-j|\leq w\}} = \lambda_\gamma(x_{i_w}, y_{j_w}) + min\begin{cases} CM_{DTW(i_w-1,j_w-1)} \\ CM_{DTW(i_w-1,j_w)} \\ CM_{DTW(i_w,j_w-1)} \end{cases} \quad (1)$$

Following the parameterization of the DTW algorithm recently proposed[55], let $\gamma\epsilon\mathbb{R}^+$ denote that γ is a positive real number. Then, the generalized distance metric is given as:

$$\lambda_\gamma(x_{i_w}, y_{j_w}) = \left|x_{i_w} - y_{j_w}\right|^\gamma \quad (2)$$

Where $\gamma > 1$ emphasizes large amplitude disparity, $\gamma < 1$ highlights small amplitude disparity and $\gamma = 1$ provides a balance between both[55].

The optimal warping path or function φ, with length L, derived from DTW, is the path that belongs to the set of all possible warping functions Π, where the cumulative distance metric between corresponding points in signals x and y is minimized. It can be expressed as:

$$\varphi = \arg min_{\varphi \epsilon \Pi} \sum_{(i_w, j_w) \epsilon \{|i-j| \leq w\}} CM_{DTW(i_w, j_w)} \qquad (3)$$

Where $L \geq \max(M, N)$

The distance cost D in DTW, which measures the phase/timing-invariant amplitude disparity between the signal pair, is computed as the sum of distance metric along the warping path. This cost is expressed as:

$$D = \sum_{\tau=1}^{L} CM_{DTW(\varphi_x(\tau), \varphi_y(\tau))} \qquad (4)$$

Where τ is the time index for the warp function, $\varphi_x(\tau)$ is the warping path along signal x, and $\varphi_y(\tau)$ is the warping path along signal y.

Notably, when the distance metric with $\gamma = 2$ is chosen the DTW distance cost becomes:

$$D = \sum_{\tau=1}^{L} \left| x\big(\varphi_x(\tau)\big) - y\left(\varphi_y(\tau)\right) \right|^{\gamma=2} \qquad (5)$$

This represents the energy (sum of squared aligned differences) of the difference signal $x\big(\varphi_x(\tau)\big) - y\left(\varphi_y(\tau)\right)$, and the normalized DTW distance cost D_n represents the power (mean squared aligned difference) of the difference signal, as given below:

$$D_n = \frac{1}{L} \sum_{\tau=1}^{L} \left| x\big(\varphi_x(\tau)\big) - y\left(\varphi_y(\tau)\right) \right|^{\gamma=2} \qquad (6)$$

This positions the algorithm as a measure of as a measure of timing-invariant signal-energy disparity between two signals (energy or power depending on normalization). Leveraging the γ −parameterization, DTW and nDTW tune sensitivity to amplitude differences $\gamma > 1$ upweights large disparities, $\gamma < 1$ upweights small disparities and $\gamma = 1$ offers the perfect balance. At $\gamma = 2$, DTW gives the conventional energy (sum of squares) of the aligned difference and nDTW gives the power (mean square).

We define convergence as relatively low nDTW (smaller power of the aligned difference), and divergence as high nDTW (larger power of the aligned difference).

4.2. Allowable window size for fMRI application

The two main challenges of DTW are its computational cost, with a time complexity of $O(M \times N)$, and the issue of singularities[19], where a single time point in one signal is unnaturally matched to a large portion of the other signal. Both challenges are mitigated by constraining the alignment to a window size that limits the maximum window of allowable alignment[56]. Given the focus on temporal deformations such as leads/lags and

nonlinear dynamics like stretching and shrinking, selecting an appropriate window size to capture relevant temporal deformations in fMRI data is crucial. In our previous study using the proposed warp elasticity approach, we demonstrated that stretching and shrinking dynamics could introduce anti-correlations[24]. Considering that anti-correlations may also arise from lead/lag relationships, it is intuitive to choose a window size that spans the length of the signal required to produce maximum anti-correlations (-1). This approach has also been validated as optimal in prior fMRI studies[21]. The longest wavelength yielding an anti-correlation of -1 corresponds to the lowest frequency component $(0.01Hz)$, which equates to a 100-second window. Achieving an anti-correlation of -1, requires a time shift of half the wavelength (50 seconds). For the DTW algorithm to capture relevant temporal deformations in fMRI data, two 50-second windows are sufficient to account for deformations in both directions, resulting in a total window length of 100 seconds[21], corresponding to the low-cutoff frequency of $0.01Hz$. However, since the filter design for the data, commonly Butterworth, is typically nonideal, we instead recommend selecting a window size based on the spectral characteristics of the activity signal, determined by the $-3db$ point of the low-frequency cutoff of the fMRI signal[13,23,24,57]. The equation for determining the window size is:

$$f_{3db} = \frac{0.88}{\sqrt{N^2 - 1}} F_s \tag{7}$$

Where N represents the number of points in the window, F_s denotes the sampling frequency, and f_{3db} is the low cutoff frequency.

4.3. Time-resolved DTW

To derive a time-resolved evolution of signal-energy imbalances, we modify the nDTW measure by eliminating its summation and normalization components. This yields a time-resolved signal-energy mismatch metric, $D_{tr}(\tau)$, for the aligned signals, ensuring that its average corresponds to the original nDTW value. The formulations are as follows:

$$\begin{gathered} D_{tr}(\tau) = \left| x\big(\varphi_x(\tau)\big) - y\left(\varphi_y(\tau)\right) \right|^{\gamma} \\ D_n = \frac{1}{L} \sum_{\tau=1}^{L} D_{tr}(\tau) \end{gathered} \tag{8}$$

However, the DTW algorithm results in aligned signal lengths L that vary across different signal pairs, complicating comparisons between brain network pairs. To ensure that the length of the time-resolved metric equals the signal length and averages to the nDTW, it is necessary to interpolate $D_{tr}(\tau)$ with the warped time scale (τ) to have the same length as the original time index (t), N or M (noting that $N = M$). This interpolation must preserve the integrity of the metric, particularly the first derivatives of the warping functions, which are crucial for capturing the varying temporal scales of fMRI time series as established in our previous study[24].

To address this, we employed the piecewise cubic Hermite interpolating polynomial (PCHIP) method for interpolating $D_{tr}(\tau)$ to the original signal length N. PCHIP was selected for its ability to preserve the shape and monotonicity[58] of the original warping functions, thereby maintaining the temporal dynamics of the fMRI signals. Unlike standard cubic splines, PCHIP avoids introducing artificial oscillations and overshoots[58], ensuring the fidelity of the signal-energy mismatch measurements. Additionally, PCHIP guarantees continuous first derivatives[58], aligning with our requirement to maintain the derivatives of the warping functions. This interpolation ensures that the interpolated metric $D_{tr}^{pchip}(\tau)$ accurately averages to the D_n, facilitating consistent and comparable analyses across all brain network pairs.

The interpolated time-resolved DTW metric is thus defined as:

$$D_{tr}^{pchip}(\tau) = PCHIP\big(D_{tr}(\tau)\big),\ \ where\ |\tau| = N = M$$
$$D_n \approx \frac{1}{N}\sum_{\tau=1}^{N} D_{tr}^{pchip}(\tau) \tag{9}$$

To validate our approach, we generated 10,000 independent and identically distributed (i.i.d.) Gaussian signal pairs, each sampled from a standard normal distribution $\mathcal{N}(0,1)$. Calculating the percentage relative difference between the nDTW and the average time-resolved DTW yielded a median percentage difference of 0.20% (Supplementary Material).

This methodology ensures that the time-resolved metric retains its temporal dynamics and derivative continuity while standardizing its length. Consequently, preserving D_n within the time-resolved measure maintains its reliability, thereby enhancing the robustness of our analysis.

4.4. Resting-state fMRI data

The first dataset used is from the Function Biomedical Informatics Research Network (fBIRN) study including resting fMRI data collected from schizophrenia patients and controls[59]. Scans were collected at a repetition time (TR) of 2 seconds. The study led to a total of 160 controls with an average age of 37.04 ± 10.86 years, ranging from 19 to 59 years. Among these, 45 were female and 115 were male. Additionally, there were 151 patients diagnosed with schizophrenia, with an average age of 38.77 ± 11.63 years, ranging from 18 to 62 years. In this group, 36 were female and 115 were male. The typical controls and schizophrenic patients were meticulously matched in terms of age, gender distribution, and mean framewise displacement during scans (age: $p = 0.18$; gender: $p = 0.39$; mean framewise displacement: $p = 0.97$). Schizophrenic patients were in a clinically stable condition during the time of their scans. The fBIRN dataset is used in all the clinical analysis performed in this study.

The second dataset used in our study is the resting-state fMRI dataset collected from 827 subjects via the Human Connectome Project (HCP) database[60,61]. We utilized both session scans acquired using a Siemens Skyra 3T scanner with a multiband accelerated, gradient-echo echo-planar imaging (EPI) sequence. The scanning parameters were set to a TR of 0.72s, 72 slices, an echo time (TE) of 58ms, and a flip angle of 90°. A voxel size of 2 × 2 × 2 mm was used to acquire 1200 time points of fMRI data for each subject. The HCP dataset was used for our test-retest analysis.

4.5. Resting-state fMRI pre-processing

fMRI data requires extensive preprocessing to correct for various sources of noise and artifacts before analysis. The preprocessing steps commonly applied in fMRI studies include slice timing correction, realignment, spatial normalization, and spatial smoothing[62]. Following typical preprocessing[63], we implemented the NeuroMark pipeline, a fully automated spatially constrained ICA on the preprocessed fMRI data[64]. Using the neuromark_fMRI_1.0 template (available in GIFT at http://trendscenter.org/software/gift or http://trendscenter.org/data), we generated 53 intrinsic connectivity networks (ICNs) for each subject. These ICNs are grouped into brain functional domains, including subcortical, auditory, sensorimotor, visual, cognitive control, default mode, and cerebellum.

4.6. Resting-state fMRI post-processing

To enhance the quality of these ICNs, we implemented detrending and despiking methods to eliminate drifts, sudden fluctuations, and significant artifacts that may have persisted after the initial preprocessing stages. The time series of the ICNs were bandpass filtered within two frequency ranges: F1 (0.01-0.198Hz) and F2(0.01-0.15Hz). An infinite impulse response filter was designed using the butter function in MATLAB and applied via the *filtfilt* function to ensure zero phase shifts and preserve phase information. The optimal filter order was estimated using the *Buttord* function in MATLAB, which returns the lowest order of the Butterworth filter with no more than 3dB ripple in the passband and at least 30dB of attenuation in the stopband. Finally, we performed z-scoring on the ICNs. The MATLAB version used was MATLAB R2022a for all steps of the analysis.

4.7. Test-retest reliability

Typically, test-retest reliability is evaluated using the intra-class correlation coefficient (ICC). However, the ICC relies on a linear parametric ANOVA model that assumes separability and additivity[65]. This makes ICC unsuitable for DTW applications, as DTW generates a distance metric based on nonlinear warping, where pairwise distances are interdependent[21,22] and thus lack decomposable variance components. We utilize the HCP dataset, which includes two sessions and a large sample size of 827 subjects, facilitating robust test-retest analysis.

4.7.1. Within-subject variability

We adopt the approach of a previous study by employing a straightforward method to assess within-subject variability: a paired sample t-test between sessions for each brain network pair[21]. The absolute t-value is reported as a measure of how much the differences between the two sessions deviate from zero, where lower absolute t-values indicate higher within-subject consistency. The formula for calculating the absolute t-value between two sessions of a single network pair across all subjects is provided below:

$$|t|_{within} = \left|\frac{\bar{d}}{s_d/\sqrt{n}}\right| \qquad (10)$$

Where $\bar{d}$ is the mean difference between two sessions, s_d is the standard deviation of the differences, and n is the total number of subjects.

4.7.2. Between-subject variability

To assess between-subject variability, we developed a non-parametric equivalent of the absolute t-value. First, we calculate the differences between the means of each subject's distribution to capture variability across the group. Since the direction of these differences is not of primary interest, we take their absolute values, resulting in a distribution skewed toward zero. This transformation allows us to perform a non-parametric test to evaluate how a non-parametric central tendency measure, such as the median, deviates from zero. Unlike the parametric approach, which scales the central tendency measure by the standard deviation, our non-parametric method scales it by the interquartile range to account for the skewed distribution. The formula for the non-parametric absolute variability measure for a single session is as follows:

$$d_i = |s_{1,i} - \bar{s_1}|$$
$$|t|_{between} = \left|\frac{median(d)}{IQR(d)/\sqrt{n}}\right| \qquad (11)$$

Where d_i is the absolute difference between subject i's measure in session 1 ($s_{1,i}$) and the group mean for session 1 ($\bar{s_1}$), $IQR(d)$ is the interquartile range of the differences d, and n is the total number of subjects.

This non-parametric approach provides a robust measure of between-subject variability that is less influenced by outliers and non-normal distributions, thereby enhancing the reliability of our variability assessments.

4.7.3. Composite test-retest reliability score

To further summarize these two approaches to give a wholistic view of test-retest reliability, we compute a composite score of test-retest as follows:

$$trt = 1 - \frac{|t|_{within}}{|t|_{between}} \quad (12)$$

Scores approaching 1 indicate higher test-retest reliability.

In our study, we compared trt scores across various gamma values of nDTW against correlation as a benchmark. To achieve this, we ranked the trt scores and performed Wilcoxon signed-rank tests between each gamma value's trt scores and the correlation benchmark across all brain network pairs, following a critical difference computation approach.

4.8. Group difference and clinical association analyses

We employed generalized linear models for both group difference analyses and associations with clinical scores. All GLM analyses controlled for sex, age, site, and mean frame displacement. P-values were adjusted using the false discovery rate method, with significance set at a threshold of 0.05. For group difference analyses and computerized multiphasic interactive neurocognitive system scores, a normal distribution was assumed, whereas a Poisson distribution was applied for PANSS score associations due to the positive integer and skewed nature of the fBIRN dataset's PANSS scores. Effect sizes were calculated using Cohen's d.

4.9. Group difference sensitivity test

To evaluate the sensitivity of various gamma values of nDTW and correlation in distinguishing between controls and individuals with schizophrenia, we conducted McNemar's sensitivity tests comparing each gamma value and correlation against each other. Following the GLM group difference analyses, we counted the number of significant brain network pairs (FDR corrected $p < 0.05$) for each gamma value (nDTW) and for correlation. We then compared the unique and shared significant pairs between each gamma and correlation using McNemar's test, with p-values adjusted via FDR correction across all comparisons.

These sensitivity tests were performed separately for each frequency range, F1 and F2. Additionally, we compared F1 and F2 across all gamma values and correlation metric to assess how transitioning from the lower frequency range F2 to the broader F1 range affects group difference sensitivity.

4.10. Validation of high fMRI frequency results.

High-frequency fMRI signals are vulnerable to various sources of noise and artifacts, including physiological factors like respiratory and cardiac activity, as well as non-neuronal influences such as head motion[66]. Comprehensive preprocessing steps followed by our use of ICA help mitigate these concerns. ICA effectively separates independent components, allowing us to identify and remove artifact-related components

from the data. Additionally, we included head motion parameters as covariates in our GLM analyses to ensure that detected group differences in high-frequency signals are not attributable to head motion effects.

We conducted several additional analyses to further validate our findings within the F1 frequency range.

4.10.1. Statistical effects on groups with the inclusion of fast BOLD fluctuations

We aimed to evaluate the impact of transitioning from the F2 to the broader F1 frequency range on both control and schizophrenia groups. Since F1 and F2 comprise the same dataset differentiated only by frequency range, a paired sample t-test was appropriate for this analysis. To validate the use of the paired t-test, we first assessed the normality of nDTW scores for each group between F1 and F2 using the Shapiro-Wilk test, ensuring that t-values were close to 1.

Subsequently, we conducted paired t-tests separately for the control and schizophrenia groups to examine the effects of transitioning from F2 to F1, with p-values adjusted using the FDR correction. Effect sizes for these comparisons were calculated using Cohen's d. Additionally, to highlight the differential impact of transitioning from F2 to F1 between groups, we computed the differences in Cohen's d effect sizes between controls and schizophrenia. This comparison aimed to determine whether the transition to the broader F1 frequency range enhances or diminishes group-specific distinctions.

Furthermore, we identified statistical group differences between schizophrenia and controls that were present in F1 but not in F2 by analyzing the shared and unique significant brain network pairs from our GLM analysis (see Section 3.7). We also highlighted their corresponding effect sizes, demonstrating that significant group differences are more pronounced in the F1 frequency range.

4.10.2. Null hypothesis test

The phase randomization (PR) technique generates surrogate fMRI data by preserving the correlation between brain network pairs[67]. This method is suitable for fMRI null hypothesis testing as it assesses non-stationarity by capturing information beyond linear and static correlations[67]. In our previous study[22], we employed PR to evaluate the statistical relevance of both DTW and nDTW in fMRI data, demonstrating that both metrics rejected the null hypothesis for several brain region pairs. This validation confirms that the DTW and nDTW methods are sensitive to capturing information beyond traditional correlation measures.

In this study, we utilize PR to assess the statistical relevance of nDTW in capturing non-stationary amplitude changes specifically due to the inclusion of higher frequency data (0.15–0.198 Hz). The following steps were followed to generate 1,000 surrogate fMRI datasets:

I. Phase Randomization**:** Apply PR to the F1 frequency range data (0.01–0.198 Hz) to create surrogate data, denoted as Z.

II. Filtering Z: Use the designed filter applied to achieve original F2 fMRI data (see section 3.4.) on Z to extract the 0.01–0.15 Hz frequency range of the surrogate data, resulting in surrogate data Y.

III. Isolating Higher Frequencies: Subtract Y from Z to obtain the surrogate data residual high frequency 0.15–0.198 Hz, denoted as X.

IV. Full surrogate data: Add X to the original F2 fMRI data (0.01–0.15 Hz) to generate surrogate data with phase randomization affecting only the residual 0.15–0.198 Hz frequency range.

This process generates surrogate datasets where randomization impacts solely the residual 0.15–0.198 Hz frequency range. A high-pass filter was not applied on Z to obtain the 0.15–0.198 Hz surrogate data because non-ideal filters will artificially create frequency multiples at the edges (~0.15 Hz).

We performed a Wilcoxon rank-sum test (FDR-corrected $p < 0.05$) to compare nDTW scores from the original fMRI data with those from surrogate data. This test assessed whether the significant brain network pairs distinguishing controls from schizophrenia, identified exclusively in the F1 range, also rejected the null hypothesis.

4.10.3. PANSS association exclusive to F1

We identified significant brain network pairs associated with symptom scores that were exclusive to the F1 frequency range and not present in the F2 range.

4.11. Signal-energy imbalance dynamics

4.11.1. Brain state estimation

In time-resolved fMRI studies, k-means clustering is frequently utilized to identify recurring brain states within the temporal dynamics of the data[68]. The DTW algorithm inherently anchors the first and last time points during alignment, potentially introducing bias by disproportionately influencing brain states at the temporal extremes. To mitigate this bias, we excluded the first and last 5 time points from the time-resolved DTW metrics prior to clustering. This exclusion reduces alignment-induced artifacts, enabling the clustering algorithm to more accurately capture intrinsic transitions between brain states.

We concatenated the time-resolved DTW metrics from all subjects in the fBIRN dataset into a single feature matrix, where each time point from every subject serves as an individual sample and each brain network pair constitutes a distinct feature. We implemented the k-means algorithm with cluster numbers ranging from 1 to 10, setting the maximum number of iterations to 10,000 and using 20 random initializations to ensure robust convergence. The city-block (Manhattan) distance metric was selected for its

demonstrated robustness in handling high-dimensional data[69]. To determine the optimal number of clusters, we generated an elbow plot based on the within-cluster sum of squares (WSS). The optimal cluster number was identified as 3, corresponding to the first significant inflection point in the WSS curve's first derivative.

4.11.2. Markov chain & stationary distribution

We quantified the transitions between brain states by counting the number of times each subject moved from one state to another and normalizing these counts across each state to construct individual transition probability matrices. This represents the probability of a subject transitioning from one state to another and further provides insights into the Markov chain of state dynamics. To gain a comprehensive understanding of the general transition patterns independent of specific groups, such as patients and controls, we aggregate the probability transitions across all subjects in the fBIRN dataset.

Furthermore, the stationary distribution of the Markov chain represents the long-term behavior of the system, indicating the proportion of time the system spends in each state once it has converged to equilibrium[70]. This distribution serves as an indication of a "stable point" when analyzing systems from the perspective of their Markov chains rather than traditional state-space representations. For the stationary distribution to be unique and ensure convergence from any initial state, the Markov chain must be ergodic[71]. A Markov chain is considered ergodic if it is irreducible (it is possible to get from any state to any other state, aperiodic (the system does not cycle in a fixed pattern), and positive recurrent (the expected return time to each state is finite).

The stationary distribution π is computed by solving the following system of linear equations:

$$\pi P = \pi$$

$$\sum_{k=1}^{K} \pi_k = 1 \tag{13}$$

Where $\pi = [\pi_1, \pi_2, \dots, \pi_k]$ is the stationary distribution vector, P is the transition probability matrix of the Markov chain, K is the number of distinct states from K-means (3 in our study).

4.11.3. Convergence analysis

How fast a chain takes to reach the stationary distribution gives a similar equivalent meaning to how fast a system takes to reach its stable point from any given state of the system. The spectral gap gives the rate of this convergence to equilibrium[70]. A larger spectral gap implies faster convergence rate to the stationary distribution. It is computed as follows:

$$\gamma_s = \lambda_1 - \lambda_2 \quad (14)$$

Where λ_1, and λ_2 are the largest and second largest eigen values of the Markov chain respectively. When the chain is ergodic, $\lambda_1 = 1$.

Beyond the spectral gap, the mixing time provides a more comprehensive measure of how quickly the chain approaches equilibrium[70]. The mixing time quantifies the number of steps required for the chain's state distribution to approach the stationary distribution within a specified tolerance level. A prevalent method for determining the mixing time leverages the total variation (TV) distance, which offers a rigorous metric for assessing the divergence between two probability distributions. The total variation distance at time step t is defined as:

$$\|\mu P^t - \pi\|_{TV} = \frac{1}{2}\sum_{k=1}^{K} |\mu P^t(k) - \pi(k)| \quad (14)$$

Where μ is the initial probability distribution, P^t represents its t-th power of transition matrix, indicating the state probabilities after t transitions, $\pi(k)$ is the stationary probability of state k and K is the total number of distinct states.

The mixing time, denoted as t_{MT}, is the smallest positive integer t for which the TV distance falls below a predefined tolerance level tol:

$$t_{MT} = min\{t \in \mathbb{R}^+ \mid \|\mu P^t - \pi\|_{TV} \leq tol\} \quad (15)$$

For our analysis, we set the tolerance level to $tol = 10^{-3}$. We also find the mixing time using the initial probability distribution μ farthest from the stationary distribution.

These metrics, spectral gap and mixing time, are instrumental in understanding the dynamic behavior of brain network states. The spectral gap provides insight into the inherent convergence rate of the system, while the mixing time offers a tangible measure of how quickly the system reaches equilibrium. Together, they facilitate a comprehensive analysis of signal-energy imbalances and their temporal evolution within the fMRI data, enhancing the robustness and reliability of our findings.

4.11.4. Entropy rate

We investigated how the trDTW metric inform the flexibility or rigidity of the brain's signal-energy dynamic configuration by analyzing the entropy rate. The entropy rate is defined as the limit of the average entropy per step as the number of steps approaches infinity. For an ergodic Markov chain, the entropy rate in bits can be mathematically expressed as:

$$H = -\sum_{i=1}^{K} \pi(i) \sum_{j=1}^{K} P(i,j) log_2 P(i,j) \qquad (16)$$

Where $\pi(i)$ is the stationary probability of being in state i and $P(i,j)$ is the transition probability from state i to state j.

The maximum entropy rate for $K = 3$ states is:

$$H_{max} = \log_2(3) = 1.585\ bits \qquad (17)$$

In our study, we present entropy rate as a percentage of H_{max} to enhance interpretability.

The entropy rate provides insight into the balance between order and randomness within the signal-energy imbalance dynamics. A low percentage entropy rate indicates strong order in the dynamics. Conversely, a high percentage entropy rate signifies a high degree of randomness, suggesting unpredictable signal-energy dynamics between brain networks.

4.11.5. Impact of transition probabilities on Markov chain convergence and entropy rate.

To evaluate how specific transitions within the Markov chain influence the convergence and entropy rates of the dynamics, we systematically perturbed the aggregated transition matrix. This process involved incrementally increasing the probability of individual transition cells and subsequently renormalizing the corresponding rows to ensure that each row's probabilities sum to one. Consequently, the targeted transition's probability increased while the probabilities of other transitions within the same row decreased.

For each perturbed transition, we recalculated both the spectral gap and the entropy rate to determine their percentage relative changes compared to the original values. This perturbation procedure was applied to every transition cell across 10,000 random samples, with perturbation magnitudes ranging from 10^{-1} to 10^{-3} on a logarithmic scale to ensure uniform sampling. To maintain comparability between transitions, each sample employed a single perturbation magnitude uniformly across all transition cells.

4.12. Time-resolved DTW group difference: schizophrenia vs controls

To assess the clinical relevance of the time-resolved DTW measure, we conducted group difference analyses on several derived metrics: state transitions, stationary distribution, spectral gap, mixing time, and entropy rate (see Section 3.11). Unlike the aggregated approach in Section 3.11, these metrics were calculated individually for each subject. To ensure the uniqueness of these results, we excluded subjects with non-ergodic state transitions.

Additionally, we included mean dwell time and occupancy rate in our group comparisons. Mean dwell time quantifies the average duration a subject remains in a particular state once entered[72], reflecting the persistence of states within the Markov chain. Occupancy rate represents the percentage of time a subject spends in each state[72], indicating the relative prevalence of states during the observation period.

Using these subject-specific metrics, we distinguished schizophrenia patients from control subjects and performed group difference analyses employing a GLM, as described in Section 3.8. FDR correction is applied to each metric across all three identified states.

4.13. CMINDS score association

Similarly, we employed a GLM, as detailed in Section 3.8, to assess associations between each metric and CMINDS scores—including speed of processing, attention vigilance, working memory, verbal learning, visual learning, and reasoning/problem solving—within the fBIRN dataset. To account for potential group effects, separate GLM analyses were conducted for each group. For transition probabilities, we applied FDR correction to control for multiple comparisons across all transitions.

4.14. Directional time-resolved DTW

The derivation of DTW, nDTW, and our developed time-resolved DTW focuses on the absolute differences between aligned signal pairs, revealing signal-energy imbalances between brain networks. However, using only absolute differences obscures directional information—specifically, it does not indicate which brain network has higher signal or power. Understanding this directionality is essential for designing targeted interventions that address specific flexibilities or rigidities within neural circuits.

To retain directional information, we modified the time-resolved DTW by modulating it with directional information, resulting in directional time-resolved DTW:

$$D_{tr}^{d}(\tau) = \boldsymbol{sign}\left(\left|x\left(\varphi_x(\tau)\right)\right| - \left|y\left(\varphi_y(\tau)\right)\right|\right) \times D_{tr}(\tau) \qquad (18)$$

This modification allows us to detect both the magnitude and direction of signal-energy imbalances, potentially identifying which brain network may exert greater metabolic demand relative to its counterpart. We then averaged the directional time-resolved DTW within each identified cluster, enabling the determination of brain networks that consistently display higher or lower signal-energy across states. This refined metric provides a more nuanced understanding of signal-energy disparities, offering precise insights to inform interventions aimed at modulating rigidities within specific neural pathways, thereby enhancing the efficacy of clinical treatments.

To evaluate the similarity of directional information across states, we calculated correlations between the directional time-resolved DTW metrics of each state. Additionally, we performed a Kruskal-Wallis test to determine whether the distributions of directional information differ among the three states. This dual analysis serves as a sanity check, as we anticipate distinct distributions even if their correlations are comparable.

5. DECLARATION OF COMPETING INTEREST.

None.

6. AUTHORS.

Sir-Lord Wiafe: Conceptualization, Formal analysis, Methodology, Visualization, Writing –original draft. **Spencer Kinsey:** Methodology, Validation, Writing – review & editing. **Najme Soleimani:** Validation, Writing – review & editing. **Raymond O. Nsafoa:** Validation, Supervision. **Nigar Khasayeva:** Validation, Writing – review & editing. **Amritha Harikumar:** Validation, Writing – review & editing. **Robyn Miller:** Validation, Methodology, Supervision, Writing – review & editing**. Vince Calhoun:** Funding acquisition, Validation, Methodology, Resources, Supervision, Writing – review & editing.

7. DATA & CODE AVAILABILITY STATEMENT.

The codes for all our analyses in MATLAB language can be accessed through GitHub (study code*)*. The data was not collected by us and was provided in a deidentified manner. The IRB will not allow sharing of data or individual derivatives as a data reuse agreement was not signed by the subjects during the original acquisition.

8. ACKNOWLEDGMENT.

This work was supported by the National Institutes of Health (NIH) grant (R01MH123610) and the National Science Foundation (NSF) grant #2112455.

9. REFERENCES.

1. Rolfe D, Brown GC. Cellular energy utilization and molecular origin of standard metabolic rate in mammals. *Physiological reviews.* 1997;77(3):731-758.
2. Magistretti Pierre J, Allaman I. A Cellular Perspective on Brain Energy Metabolism and Functional Imaging. *Neuron.* 2015;86(4):883-901.
3. Logothetis NK, Pauls J, Augath M, Trinath T, Oeltermann A. Neurophysiological investigation of the basis of the fMRI signal. *nature.* 2001;412(6843):150-157.
4. Raichle ME. Behind the scenes of functional brain imaging: a historical and physiological perspective. *Proceedings of the National Academy of Sciences.* 1998;95(3):765-772.
5. Tomasi D, Wang G-J, Volkow ND. Energetic cost of brain functional connectivity. *Proceedings of the National Academy of Sciences.* 2013;110(33):13642-13647.
6. Golesorkhi M, Gomez-Pilar J, Zilio F, et al. The brain and its time: intrinsic neural timescales are key for input processing. *Communications Biology.* 2021;4(1):970.

7. Buxton RB, Uludağ K, Dubowitz DJ, Liu TT. Modeling the hemodynamic response to brain activation. *Neuroimage.* 2004;23 Suppl 1:S220-233.
8. Zang YF, He Y, Zhu CZ, et al. Altered baseline brain activity in children with ADHD revealed by resting-state functional MRI. *Brain Dev.* 2007;29(2):83-91.
9. Zou QH, Zhu CZ, Yang Y, et al. An improved approach to detection of amplitude of low-frequency fluctuation (ALFF) for resting-state fMRI: fractional ALFF. *J Neurosci Methods.* 2008;172(1):137-141.
10. Fu Z, Tu Y, Di X, et al. Characterizing dynamic amplitude of low-frequency fluctuation and its relationship with dynamic functional connectivity: An application to schizophrenia. *NeuroImage.* 2018;180:619-631.
11. Allen EA, Damaraju E, Plis SM, Erhardt EB, Eichele T, Calhoun VD. Tracking whole-brain connectivity dynamics in the resting state. *Cereb Cortex.* 2014;24(3):663-676.
12. Zhang G, Cai B, Zhang A, et al. Estimating Dynamic Functional Brain Connectivity With a Sparse Hidden Markov Model. *IEEE Trans Med Imaging.* 2020;39(2):488-498.
13. Wiafe S-L, Asante NO, Calhoun VD, Faghiri A. Studying time-resolved functional connectivity via communication theory: on the complementary nature of phase synchronization and sliding window Pearson correlation. *bioRxiv.* 2024:2024.2006. 2012.598720.
14. Chang C, Glover GH. Time–frequency dynamics of resting-state brain connectivity measured with fMRI. *NeuroImage.* 2010;50(1):81-98.
15. Mitra A, Snyder AZ, Hacker CD, Raichle ME. Lag structure in resting-state fMRI. *J Neurophysiol.* 2014;111(11):2374-2391.
16. Thapaliya B, Akbas E, Chen J, et al. Brain networks and intelligence: A graph neural network based approach to resting state fmri data. *Medical Image Analysis.* 2025;101:103433.
17. Thapaliya B, Wu Z, Sapkota R, et al. Graph-based deep learning models in the prediction of early-stage Alzheimers. Paper presented at: 2024 46th Annual International Conference of the IEEE Engineering in Medicine and Biology Society (EMBC)2024.
18. Thapaliya B, Miller R, Chen J, et al. DSAM: A deep learning framework for analyzing temporal and spatial dynamics in brain networks. *Medical Image Analysis.* 2025:103462.
19. Sakoe H, Chiba S. Dynamic programming algorithm optimization for spoken word recognition. *IEEE Transactions on Acoustics, Speech, and Signal Processing.* 1978;26(1):43-49.
20. Linke AC, Mash LE, Fong CH, et al. Dynamic time warping outperforms Pearson correlation in detecting atypical functional connectivity in autism spectrum disorders. *NeuroImage.* 2020;223:117383.
21. Meszlényi RJ, Hermann P, Buza K, Gál V, Vidnyánszky Z. Resting State fMRI Functional Connectivity Analysis Using Dynamic Time Warping. *Frontiers in Neuroscience.* 2017;11.
22. Wiafe S-L, Kinsey S, Iraji A, Miller R, Calhoun VD. Normalized Dynamic Time Warping Increases Sensitivity In Differentiating Functional Network Connectivity In Schizophrenia. *bioRxiv.* 2024:2024.2010.2031.621415.
23. Wiafe S-L, Faghiri A, Fu Z, Miller R, Calhoun V. *Capturing Stretching and Shrinking of Inter-Network Temporal Coupling in FMRI Via WARP Elasticity.* 2024.
24. Wiafe S-L, Faghiri A, Fu Z, Miller R, Preda A, Calhoun VD. The dynamics of dynamic time warping in fMRI data: a method to capture inter-network stretching and shrinking via warp elasticity. *Imaging Neuroscience.* 2024.
25. Birn RM, Cornejo MD, Molloy EK, et al. The influence of physiological noise correction on test-retest reliability of resting-state functional connectivity. *Brain Connect.* 2014;4(7):511-522.
26. Lindauer U, Leithner C, Kaasch H, et al. Neurovascular coupling in rat brain operates independent of hemoglobin deoxygenation. *Journal of cerebral blood flow & metabolism.* 2010;30(4):757-768.

27. Wolf T, Lindauer U, Villringer A, Dirnagl U. Excessive oxygen or glucose supply does not alter the blood flow response to somatosensory stimulation or spreading depression in rats. *Brain research.* 1997;761(2):290-299.
28. Brown AM, Ransom BR. Astrocyte glycogen and brain energy metabolism. *Glia.* 2007;55(12):1263-1271.
29. Pellerin L, Bouzier-Sore AK, Aubert A, et al. Activity-dependent regulation of energy metabolism by astrocytes: an update. *Glia.* 2007;55(12):1251-1262.
30. Hillman EM. Coupling mechanism and significance of the BOLD signal: a status report. *Annu Rev Neurosci.* 2014;37:161-181.
31. Dwyer DS, Bradley RJ, Kablinger AS, Freeman AM, 3rd. Glucose metabolism in relation to schizophrenia and antipsychotic drug treatment. *Ann Clin Psychiatry.* 2001;13(2):103-113.
32. Newcomer JW, Haupt DW, Fucetola R, et al. Abnormalities in Glucose Regulation During Antipsychotic Treatment of Schizophrenia. *Archives of General Psychiatry.* 2002;59(4):337-345.
33. Gohel SR, Biswal BB. Functional integration between brain regions at rest occurs in multiple-frequency bands. *Brain Connect.* 2015;5(1):23-34.
34. Gatti D, Rinaldi L, Ferreri L, Vecchi T. The Human Cerebellum as a Hub of the Predictive Brain. *Brain Sci.* 2021;11(11).
35. Schmahmann JD. An emerging concept: the cerebellar contribution to higher function. *Archives of neurology.* 1991;48(11):1178-1187.
36. Andreasen NC, Paradiso S, O'Leary DS. “Cognitive dysmetria” as an integrative theory of schizophrenia: a dysfunction in cortical-subcortical-cerebellar circuitry? *Schizophrenia bulletin.* 1998;24(2):203-218.
37. Speers LJ, Bilkey DK. Maladaptive explore/exploit trade-offs in schizophrenia. *Trends in Neurosciences.* 2023;46(5):341-354.
38. Millan MJ, Fone K, Steckler T, Horan WP. Negative symptoms of schizophrenia: Clinical characteristics, pathophysiological substrates, experimental models and prospects for improved treatment. *European Neuropsychopharmacology.* 2014;24(5):645-692.
39. Gu X, Ke S, Wang Q, et al. Energy metabolism in major depressive disorder: Recent advances from omics technologies and imaging. *Biomedicine & Pharmacotherapy.* 2021;141:111869.
40. Meng F, Wang J, Wang L, Zou W. Glucose metabolism impairment in major depressive disorder. *Brain Research Bulletin.* 2025;221:111191.
41. Wu Q, Long Y, Peng X, et al. Prefrontal cortical dopamine deficit may cause impaired glucose metabolism in schizophrenia. *Translational Psychiatry.* 2024;14(1):79.
42. Biswal B, Yetkin FZ, Haughton VM, Hyde JS. Functional connectivity in the motor cortex of resting human brain using echo-planar MRI. *Magn Reson Med.* 1995;34(4):537-541.
43. DeRamus T, Faghiri A, Iraji A, et al. Modular and state-relevant functional network connectivity in high-frequency eyes open vs eyes closed resting fMRI data. *Journal of Neuroscience Methods.* 2021;358:109202.
44. Faghiri A, Iraji A, Damaraju E, Turner J, Calhoun VD. A unified approach for characterizing static/dynamic connectivity frequency profiles using filter banks. *Network Neuroscience.* 2021;5(1):56-82.
45. Gonder-Frederick LA, Zrebiec JF, Bauchowitz AU, et al. Cognitive function is disrupted by both hypo- and hyperglycemia in school-aged children with type 1 diabetes: a field study. *Diabetes Care.* 2009;32(6):1001-1006.
46. Jamadar SD, Behler A, Deery H, Breakspear M. The metabolic costs of cognition. *Trends in Cognitive Sciences.*
47. Cocchi L, Gollo LL, Zalesky A, Breakspear M. Criticality in the brain: A synthesis of neurobiology, models and cognition. *Progress in Neurobiology.* 2017;158:132-152.

48. Moretti P, Muñoz MA. Griffiths phases and the stretching of criticality in brain networks. *Nature communications.* 2013;4(1):2521.
49. Shi J, Kirihara K, Tada M, et al. Criticality in the Healthy Brain. *Front Netw Physiol.* 2021;1:755685.
50. Carhart-Harris RL. The entropic brain - revisited. *Neuropharmacology.* 2018;142:167-178.
51. Xu L, Feng J, Yu L. Avalanche criticality in individuals, fluid intelligence, and working memory. *Hum Brain Mapp.* 2022;43(8):2534-2553.
52. Roheger M, Kessler J, Kalbe E. Structured Cognitive Training Yields Best Results in Healthy Older Adults, and Their ApoE4 State and Baseline Cognitive Level Predict Training Benefits. *Cogn Behav Neurol.* 2019;32(2):76-86.
53. Friston KJ. The disconnection hypothesis. *Schizophrenia research.* 1998;30(2):115-125.
54. Paliwal KK, Agarwal A, Sinha SS. A modification over Sakoe and Chiba's dynamic time warping algorithm for isolated word recognition. *Signal Processing.* 1982;4(4):329-333.
55. Herrmann M, Tan CW, Webb GI. Parameterizing the cost function of dynamic time warping with application to time series classification. *Data Mining and Knowledge Discovery.* 2023;37(5):2024-2045.
56. Berndt DJ, Clifford J. Using Dynamic Time Warping to Find Patterns in Time Series. Paper presented at: KDD Workshop1994.
57. Faghiri A, Yang K, Ishizuka K, Sawa A, Adali T, Calhoun V. *Frequency modulation increases the specificity of time-resolved connectivity: A resting-state fMRI study.* 2023.
58. Fritsch FN, Carlson RE. Monotone piecewise cubic interpolation. *SIAM Journal on Numerical Analysis.* 1980;17(2):238-246.
59. Keator DB, van Erp TGM, Turner JA, et al. The Function Biomedical Informatics Research Network Data Repository. *Neuroimage.* 2016;124(Pt B):1074-1079.
60. Van Essen DC, Smith SM, Barch DM, Behrens TEJ, Yacoub E, Ugurbil K. The WU-Minn Human Connectome Project: An overview. *NeuroImage.* 2013;80:62-79.
61. Van Essen DC, Ugurbil K, Auerbach E, et al. The Human Connectome Project: a data acquisition perspective. *Neuroimage.* 2012;62(4):2222-2231.
62. Penny WD, Friston KJ, Ashburner JT, Kiebel SJ, Nichols TE. *Statistical parametric mapping: the analysis of functional brain images.* Elsevier; 2011.
63. Fu Z, Batta I, Wu L, et al. Searching Reproducible Brain Features using NeuroMark: Templates for Different Age Populations and Imaging Modalities. *Neuroimage.* 2024;292:120617.
64. Du Y, Fu Z, Sui J, et al. NeuroMark: An automated and adaptive ICA based pipeline to identify reproducible fMRI markers of brain disorders. *Neuroimage Clin.* 2020;28:102375.
65. Wang Z, Bridgeford E, Wang S, Vogelstein JT, Caffo B. Statistical analysis of data repeatability measures. *International Statistical Review.* 2024.
66. Murphy K, Birn RM, Bandettini PA. Resting-state fMRI confounds and cleanup. *Neuroimage.* 2013;80:349-359.
67. Liégeois R, Yeo BTT, Van De Ville D. Interpreting null models of resting-state functional MRI dynamics: not throwing the model out with the hypothesis. *NeuroImage.* 2021;243:118518.
68. Damaraju E, Allen EA, Belger A, et al. Dynamic functional connectivity analysis reveals transient states of dysconnectivity in schizophrenia. *NeuroImage: Clinical.* 2014;5:298-308.
69. Aggarwal CC, Hinneburg A, Keim DA. On the surprising behavior of distance metrics in high dimensional space. Paper presented at: Database Theory—ICDT 2001: 8th International Conference London, UK, January 4–6, 2001 Proceedings 82001.
70. Levin DA, Peres Y. *Markov chains and mixing times.* Vol 107: American Mathematical Soc.; 2017.
71. Basharin GP, Langville AN, Naumov VA. The life and work of A.A. Markov. *Linear Algebra and its Applications.* 2004;386:3-26.

72. Iraji A, Faghiri A, Lewis N, Fu Z, Rachakonda S, Calhoun VD. Tools of the trade: estimating time-varying connectivity patterns from fMRI data. *Social Cognitive and Affective Neuroscience.* 2020;16(8):849-874.